Journal of Sound and Vibration (2001) **243**(2), 317–346
doi:10.1006/jsvi.2000.3418, available online at http://www.idealibrary.com on IDEAL®

DYNAMIC PERFORMANCE OF C-BLOCK ARRAY ARCHITECTURES

A. J. MOSKALIK

U.S. EPA—National Vehicle and Fuel Emissions Laboratory, 2000 *Traverwood Dr.*, *Ann Arbor*, *MI* 48105, *U.S.A.*

AND

D. BREI

Department of Mechanical Engineering, *The University of Michigan*, 2250 *G. G. Brown Building*, 2350 *Hayward St.*, *Ann Arbor*, *MI* 48109-2125, *U.S.A.*

(*Received* 28 *January* 2000, *and in final form* 6 *November* 2000)

The lack of adequate actuators has often been cited as the limiting factor in practical applications of smart structures. C-blocks are a building block actuation architecture that addresses the stroke limitations of stack architectures and the force limitations of bender architectures. Because these actuators are based upon piezoelectric materials, they are well suited for high bandwidth dynamic applications. This paper presents an investigation of the dynamic behavior of a generic C-block array architecture using analytical models derived from a unique transfer matrix method and experiments using four distinctly different types of prototypes. To gain insight into the dynamic behavior of the actuation architecture, a parameter analysis based upon both the models and experiments is given. The behavior of long series is found to display both bending and extensional type of behaviors, which can be well approximated with an appropriate equivalent straight bender model. For shorter series, the performance is more complex and the full analytical model is required. From the analytical models derived in this paper along with the insight gained from the straight bender and parameter analysis, it is possible to design and predict the dynamic performance of a generic C-block actuator for a given application which requires a midrange piezoelectric actuator.

1. INTRODUCTION

When selecting an actuator, an engineer has the option of using conventional methods such as electromechanical or hydraulic actuators or smart material actuators such as piezoelectric or shape memory alloys. Smart materials have 100–1000 times more energy change and 10 times more energy per mass than conventional actuator technologies, such as electromagnetic, hydraulic, and pneumatic [1]. This makes them well suited for applications where the available actuation space and allowable mass severely constrains the amount of useful work the actuator can deliver to the application. Of the smart materials available, piezoelectrics are widely utilized when speed is an issue, normally where frequencies above 5 Hz are required [2]. Unfortunately, one obstacle to piezoelectric actuators is the small strain produced. To be useful, some form of amplification is required, which is usually provided by external leveraging [3–6], frequency leveraging [7, 8], or internally leveraging schemes [9–11].

0022-460X/01/220317 + 30 $35.00/0

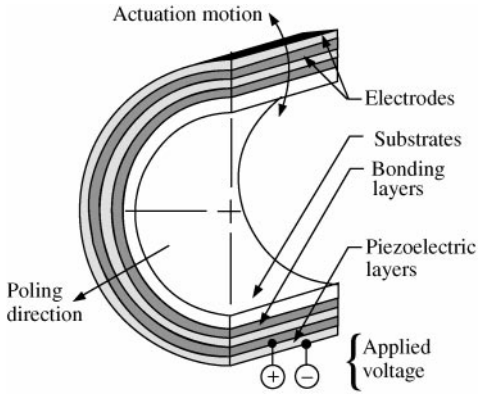

Figure 1. C-block construction. An individual C-block is constructed from multiple piezoelectric layers, electrodes, and substrates bonded together. The piezoelectrically induced strain produces a bending moment that makes the C-block flex.

A new class of piezoelectric actuators, C-blocks, is based upon an internally leveraged building-block amplification scheme. An individual building block is a C-shaped, multilayered piezoelectric bender that flexes when a voltage is applied across the thickness (Figure 1). The flexing occurs because the active piezoelectric layers are poled in the radial direction and laid up with inert layers to create a bending moment about the neutral axis when energized.

Prior research of individual C-blocks has demonstrated that C-blocks can generate 2·67 times the force of a straight bender with 40·5% of the deflection [12], thus overcoming the force limitations of benders. The deflection is two orders of magnitude greater than that of stack or externally leveraged architectures, which typically provide amplifications of only 5–25 times the bulk material strain [13]. C-blocks generate 8% more work than a straight bender constructed from the same volume of piezoelectric material [14]. This is significant considering that the straight bender is very efficient when compared to other internally leveraged architectures such as Rainbows, Crescent and Thunders [15].

The main advantage to the C-block architecture is their ability to construct distributed actuation arrays consisting of numerous individual C-blocks to further improve both the force and deflection (Figure 2) [14]. Since this is a direct extension of the architecture, C-blocks do not experience the transmission losses that can plague frequency and externally leveraged architectures by as much as a factor of three to five [13]. The series and parallel array configuration parameters give engineers two more design freedoms in addition to the geometric and material parameters that are available in other architectures. This provides a large number of feasible discrete C-block array architectures making it possible to design the actuator performance directly to the application for optimal stiffness, force, deflection and bandwidth. Thus, even though the C-block uses the d_{31} mode of the material that is inefficient for high force applications, it can be directly tailored to the application with minimal transmission losses; thereby, providing one of the highest work/mass efficiency in the midrange performance region [14]. This region is very useful for applications such as shape control of wings [16] and antennas [17], or vibration control of automotive suspensions [18, 19], engine mounts [20], helicopter rotor blades [4, 10, 21], and machine tools [22, 23].

The quasi-static performance of both individual and array C-block architectures has been studied in depth [12, 14]. However, the true value of any piezoelectric actuator is its dynamic performance. The dynamic performance of an individual C-block has been

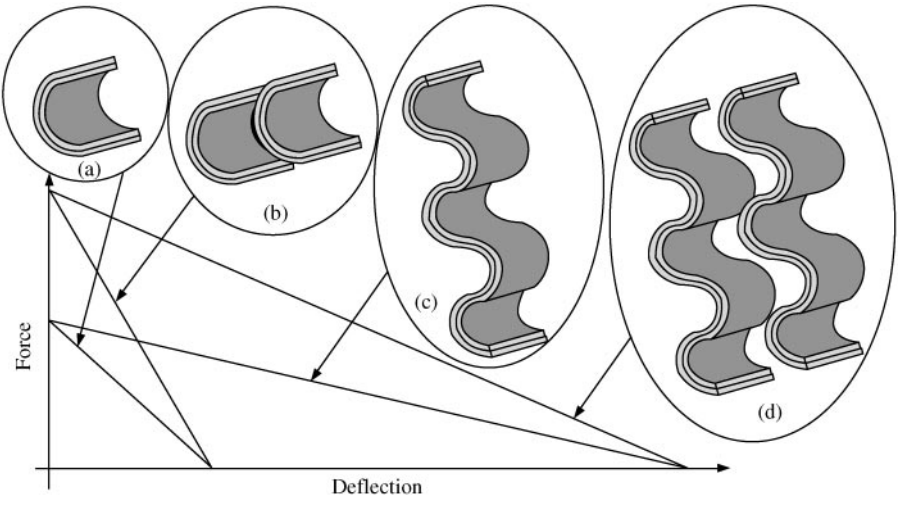

Figure 2. C-block actuator architecture configurations. (a) An individual C-block amplifies the strain of the bulk material. (b) A parallel configuration linearly increases the force with no loss in deflection. (c) A series configuration linearly increases the deflection with no loss in force. (d) An array configuration linearly increases both the force and deflection.

modelled [24]. Unfortunately, the modelling of a distributed array architecture, fabricated from a number of individual C-blocks, can be quite complex and is not a simple extension of the individual building block. In this paper, a unique modelling strategy based upon a transfer matrix method is utilized to derive an analytical model for the frequency–amplitude response of a generic C-block actuation array. This model was confirmed to be accurate through experiments using four distinctly different prototypes. The transfer matrix model is very useful for small number arrays, but is cumbersome for larger arrays. Thus, a simpler model based upon an equivalent straight beam is presented for longer series where it accurately captures the dynamic performance. The paper concludes with a parameter analysis based upon the models and experiments to investigate the sensitivity of the dynamic performance to changes in the actuation architecture.

2. C-BLOCK ARRAY ANALYTICAL PERFORMANCE MODELLING

The dynamic frequency–amplitude model for the C-block array was determined analytically using a three-step approach: (1) the equations of motion and boundary conditions for all individual C-blocks within the array were derived using Hamilton's principle. (2) From the equations of motion and boundary conditions, the exact transfer matrix for an individual C-block was formulated and multiplied together with a co-ordinate transformation matrix to determine the transfer matrix for an array C-block. (3) Using the transfer matrix method, the natural frequencies and the displacement amplitude of the C-block array were generated.

During the derivation, the C-block is assumed to be a cantilevered system with m C-blocks in parallel, and n in series, each identical, with a constant radius and total angular span of π radians. Each C-block is a thin cross-section with q layers. Thus, the electric field, E_3, within the piezoelectric material is equal to the voltage divided by the thickness of the material, $E_3 = V/(z_j - z_{j-1})$ and the effects of transverse shear and rotatory inertia are assumed negligible. Further nomenclature is shown in Figure 3, where

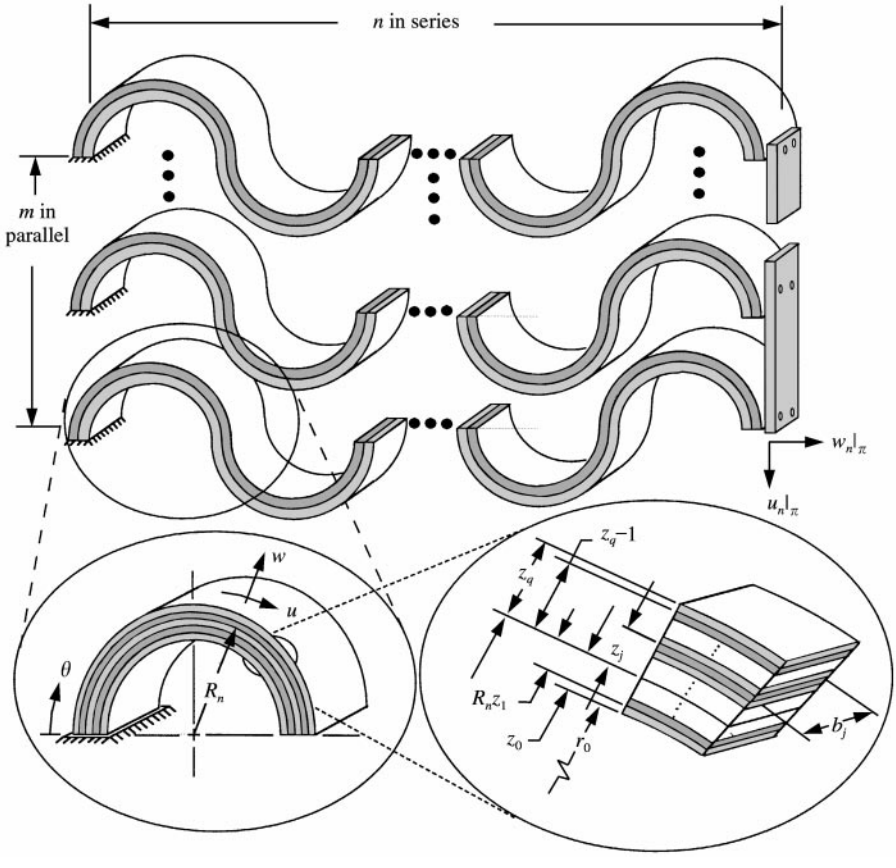

Figure 3. Geometric notation for a generic array of C-blocks. A generic array of C-blocks contains m sets of C-blocks in parallel and n sets of C-blocks in series. Each individual C-block has identical geometric and material parameters, and a tip mass and applied force are distributed evenly among the parallel elements.

u and w are the circumferential and radial deflections, respectively, θ is an angular co-ordinate, R_n is the neutral axis radius, b is a layer width, r is the distance from the C-block center to the outside of a layer, z is the distance from the neutral axis to the outside of a layer ($z = r - R_n$), and ρ is the mass per unit length. The internal damping within the C-block is modelled as structural damping, with an equivalent viscous damping coefficient, γ/Ω, inversely proportional to the forcing frequency [25].

2.1. EQUATIONS OF MOTION AND BOUNDARY CONDITIONS

The first step in developing the frequency–amplitude model is the derivation of the equations of motion. Hamilton's principle,

$$\int_{t_1}^{t_2} (\delta T - \delta U + \delta W)\,\mathrm{d}t = 0, \tag{1}$$

was employed in a form similar to that used for non-piezoelectric laminated curved beams [26] with piezoelectric terms included in the constitutive equation [27].

The strain energy, U, is derived from the internal stress and strain,

$$U = \sum_{l=1}^{m} \sum_{k=1}^{n} \frac{1}{2} \int_0^{\pi} \left[N u_{kl,\theta} + N w_{kl} - \frac{M}{R_n} w_{kl,\theta\theta} + \frac{M}{R_n} u_{kl,\theta} \right] \mathrm{d}\theta, \tag{2}$$

where u_{kl} is the circumferential displacement and w_{kl} is the radial displacement of the kth C-block in series and the lth C-block in parallel, M is the internal moment, N is the internal normal force, and the subscript ,θ refers to differentiation with respect to the circumferential co-ordinate. The kinetic energy, T, is the sum of the kinetic energy from each cross-section in the C-block,

$$T = \sum_{l=1}^{m} \sum_{k=1}^{n} \frac{\rho}{2} \int_0^{\pi} [(u_{kl,t})^2 + (w_{kl,t})^2] \, R_n \, \mathrm{d}\theta, \tag{3}$$

where ρ is the mass per unit length of the C-block and the subscript ,t refers to differentiation with respect to time. The non-conservative forces, W, are modelled as viscous damping,

$$W = \sum_{l=1}^{m} \sum_{k=1}^{n} \frac{\gamma}{2\Omega} \int_0^{\pi} \left[N u_{kl,\theta t} + N w_{kl,t} - \frac{M}{R_n} w_{kl,\theta\theta t} + \frac{M}{R_n} u_{kl,\theta t} \right] \mathrm{d}\theta, \tag{4}$$

where γ is the non-dimensional damping coefficient and Ω is the forcing frequency. This work term is the time derivative of the strain energy term (equation (2)) with a multiple of γ/Ω.

The moment, M, and normal force, N, are associated with individual C-blocks, and are the same here as in the individual C-block derivation [24],

$$\begin{Bmatrix} N \\ M \end{Bmatrix} = \begin{bmatrix} A & 0 \\ 0 & D \end{bmatrix} \begin{Bmatrix} \varepsilon^0 \\ \kappa \end{Bmatrix} + \begin{Bmatrix} N^P \\ M^P \end{Bmatrix}, \tag{5}$$

where the extensional stiffness, A, and bending stiffness, D, are defined as

$$A = \sum_{j=1}^{q} Y_j b_j (z_j - z_{j-1}) \quad \text{and} \quad D = \sum_{j=1}^{q} \frac{1}{3} Y_j b_j (z_j^3 - z_{j-1}^3), \tag{6}$$

the piezoelectric normal force, N^P, and piezoelectric moment, M^P, are defined as

$$N^P = \sum_{j=1}^{q} Y_j b_j (z_j - z_{j-1})(d_{31} E_3)_j \quad \text{and} \quad M^P = \sum_{j=1}^{q} \frac{1}{2} Y_j b_j (z_j^2 - z_{j-1}^2) (d_{31} E_3)_j \tag{7}$$

and the relationships among the circumferential deflection, u_{kl}, radial deflection, w_{kl}, strain, ε^0, and curvature change, κ are

$$\varepsilon^0 = \frac{1}{R_n} (u_{kl,\theta} + w_{kl}), \quad \kappa = \frac{1}{R_n^2} (- w_{kl,\theta\theta} + u_{kl,\theta}). \tag{8}$$

In these equations, Y is the Young's modulus of the material, z is the distance to the neutral axis, b is the width, and $d_{31}E_3$ is the internally induced piezoelectric strain.

The variations of the strain energy (equation (2)), kinetic energy (equation (3)), and work terms (equation (4)) are added together to produce an expression for Hamilton's principle

for an array of n C-blocks in series and m in parallel,

$$\sum_{l=1}^{m} \int_{t_1}^{t_2} \left\{ \begin{array}{l} \displaystyle\sum_{k=1}^{n} \int_0^{\pi} \left[\begin{array}{l} -R_n \rho u_{kl,tt}\, \delta u_{kl} - R_n \rho w_{kl,tt}\, \delta w_{kl} + N_{,\theta}\, \delta u_{kl} - N\, \delta w_{kl} + \dfrac{M_{,\theta\theta}}{R_n}\, \delta w_{kl} \\ + \dfrac{M_{,\theta}}{R_n}\, \delta u_{kl} + \dfrac{\gamma}{\Omega} \left(N_{,\theta}\, \delta u_{kl,t} - N\, \delta w_{kl,t} + \dfrac{M_{,\theta\theta}}{R_n}\, \delta w_{kl,t} + \dfrac{M_{,\theta}}{R_n}\, \delta u_{kl,t} \right) \end{array} \right] \mathrm{d}\theta \\ + \displaystyle\sum_{k=1}^{n} \left[\begin{array}{l} -N\, \delta u_{kl} + \dfrac{M}{R_n}\, \delta w_{kl,\theta} - \dfrac{M_{,\theta}}{R_n}\, \delta w_{kl} - \dfrac{M}{R_n}\, \delta u_{kl} \\ - \dfrac{\gamma}{\Omega} \left(N\, \delta u_{kl,t} - \dfrac{M}{R_n}\, \delta w_{kl,\theta t} + \dfrac{M_{,\theta}}{R_n}\, \delta w_{kl,t} + \dfrac{M}{R_n}\, \delta u_{kl,t} \right) \end{array} \right]_0^{\pi} \end{array} \right\} \mathrm{d}t = 0. \tag{9}$$

Equation (9) is similar in form to Hamilton's principle for an individual C-block [24], but it contains summations over n and m, thus producing a large number of equations of motion which all must be solved simultaneously.

2.1.1. *Equations of motion*

Hamilton's principle (equation (9)) is manipulated to determine the equations of motion and the associated boundary conditions for the C-block. The resulting equations are m identical sets of equations of motion and boundary conditions, and, by inspection, the solutions to these sets of differential equations will be identical. Thus, only one set of equations, representing a series of C-blocks, need be solved to determine the final behavior of the entire array. Therefore, the summation over l is dropped from equation (9), and the solution is performed on only one set of equations representing a serial C-block.

For the serial C-block, there are n sets of equations of motion, one set for each C-block within the series. Since δu_k and δw_k are arbitrary, the terms multiplying them must be zero, and form the equations of motion. These equations of motion are simplified by substituting the definitions of the moment and normal force (equation (5)), the relations between the displacement and the extensional strain and curvature change (equation (8)):

$$\left(\frac{1}{\chi} + 1\right) u_{k,\theta\theta} + \frac{1}{\chi} w_{k,\theta} - w_{k,\theta\theta\theta} + \frac{\gamma}{\Omega} \left[\left(\frac{1}{\chi} + 1\right) u_{k,\theta\theta} + \frac{1}{\chi} w_{k,\theta} - w_{k,\theta\theta\theta} \right]_{,t} = \frac{R_n^4}{D} \rho u_{k,tt}$$

$$u_{k,\theta\theta\theta} - \frac{1}{\chi} u_{k,\theta} - \frac{1}{\chi} w - w_{k,\theta\theta\theta\theta} + \frac{\gamma}{\Omega} \left[u_{ki,\theta\theta\theta} - \frac{1}{\chi} u_{k,\theta} - \frac{1}{\chi} w_k - w_{k,\theta\theta\theta\theta} \right]_{,t}$$

$$= \frac{R_n^4}{D} \rho w_{k,tt} + \frac{N^P R_n^3}{D} + \frac{\gamma N_{,t}^P R_n^3}{\Omega D}, \tag{10}$$

where the non-dimensional stiffness parameter, χ, is the ratio of the bending stiffness to the extensional stiffness, and is defined as

$$\chi = D/(AR_n^2). \tag{11}$$

Therefore, each C-block in the entire array has identical equations of motion, and these equations of motion are identical to the equations of motion for an individual C-block [24].

2.1.2. *Boundary conditions*

The boundary conditions are determined from Hamilton's principle by separating the terms outside of the spatial integral with respect to the variance each term multiplies. At the base ($\theta = 0$) of the first C-block, the displacements, u and w, and the slope, φ, are zero,

$$w_0|_0 = 0, \quad u_0|_0 = 0 \quad \text{and} \quad \varphi_0|_0 = (u - w_{,\theta})_0 = 0. \tag{12}$$

The slope, φ, is used rather than the first derivative of the radial displacement, $w_{,\theta}$, to simplify later calculations. At the tip of the last C-block ($\theta = \pi$), the moment, M, shear, V, and normal force, N, are all zero:

$$\begin{aligned} M_n|_\pi &= \frac{D}{R_n^2}\left[\left(-w_{n,\theta\theta} + u_{n,\theta} + \frac{M^P R_n^2}{D}\right) + \frac{\gamma}{\Omega}\left(-w_{n,\theta\theta t} + u_{n,\theta t} + \frac{M^P_{,t} R_n^2}{D}\right)\right]_\pi = 0, \\ V_n|_\pi &= \frac{D}{R_n^3}\left[(-w_{n,\theta\theta\theta} + u_{n,\theta\theta}) + \frac{\gamma}{\Omega}(-w_{n,\theta\theta\theta t} + u_{n,\theta\theta t}) + \frac{F_y R_n^3}{D}\right]_\pi = 0, \\ N_n|_\pi &= \frac{D}{R_n^3}\left[\left(u_{n,\theta} + w_n + \frac{N^P \chi R_n^3}{D}\right) + \frac{\gamma}{\Omega}\left(u_{n,\theta t} + w_{n,t} + \frac{N^P_{,t} \chi R_n^3}{D}\right)\right]_\pi = 0. \end{aligned} \tag{13}$$

Additionally, at the $(n-1)$ boundaries between adjacent C-blocks, all physical quantities must match:

$$\begin{gathered} u_{k+1}|_0 = u_k|_\pi, \quad w_{k+1}|_0 = -w_k|_\pi, \quad \varphi_{k+1}|_0 = -\varphi_k|_\pi, \quad M_{k+1}|_0 = -M_k|_\pi, \\ V_{k+1}|_0 = -V_k|_\pi, \quad \text{and} \quad N_{k+1}|_0 = N_k|_\pi. \end{gathered} \tag{14}$$

The n sets of equations of motion (10) and $6n$ boundary conditions (equations (12)–(14)) completely describe the behavior of the serial C-block.

2.2. TRANSFER MATRIX METHOD

As the number of C-blocks in the series increases, the number of equations of motion and boundary conditions also increase. If the equations of motion are solved simultaneously, the complexity of the solution procedure becomes formidable as the number of C-blocks in the series increases. Fortunately, there is an alternative solution method: the transfer matrix method. The transfer matrix method is a powerful tool for dynamic and static analysis, particularly for structures constructed from a series of elements linked together end to end [28]. The power of the method lies in the fact that, unlike the finite element method, the order of the matrix does not increase as the number of elements in the structure increases [29].

The methods utilized in applying transfer matrix theory are described in detail in reference [28]. The heart of the transfer matrix method is the idea that, for any element, a transfer matrix can be developed from the equations of motion that describe the relationship among the state variables (displacements, slopes, moment, and forces) at each end of the element. Thus, the individual C-block transfer matrix, $[U_i]$, satisfies the relation

$$\{z\}|_\pi = [U_i]\,\{z\}|_0, \tag{15}$$

where the boundaries of the C-block are at $\theta = 0$ and π, and the state variable vector $\{z\}$, is defined using the quantities from the boundary conditions (equations (12)–(14)),

$$\{z\} = \{u \quad -w \quad \varphi \quad M \quad V \quad N\}^{\mathrm{T}}. \tag{16}$$

The state variables u and w are tangential and radial displacements, respectively, φ is the slope, M is the moment, V is the shear, and N is the normal force.

2.2.1. *Transfer matrix for individual C-blocks*

The form of the transfer matrix for an individual C-block is determined from the equations of motion. First, the circumferential and radial displacements u and w that solve the associated eigenvalue problem are written as an infinite series of independent solutions of the form

$$u = \sum_{i=1}^{\infty} \left[\sum_{j=1}^{6} K_{ij} C_{ij} \mathrm{e}^{r_{ij}\theta} \right] \sin \omega_i t \quad \text{and} \quad w = \sum_{i=1}^{\infty} \left[\sum_{j=1}^{6} C_{ij} \mathrm{e}^{r_{ij}\theta} \right] \sin \omega_i t, \tag{17}$$

where the constants C_{ij} and K_{ij} define the radial and circumferential modeshapes and ω_i is the ith natural frequency.

The characteristic equation associated with the equations of motion (10) is

$$r_{ij}^6 + (2 + \chi\lambda_i^2) r_{ij}^4 + (1 - \lambda_i^2 - \chi\lambda_i^2) r_{ij}^2 + \lambda_i^2 (1 - \chi\lambda_i^2) = 0, \tag{18}$$

where the non-dimensional frequency, λ_i, is

$$\lambda_i^2 = \rho\omega_i^2 R_n^4 / D. \tag{19}$$

The values of K_{ij} in the modeshapes (17) that relate the circumferential solution to the radial solution are determined as a function of r_{in} by inserting the solutions (17) back into the equations of motion (10). The state variables (equation (16)) are found by using the modeshapes (17),

$$\begin{Bmatrix} u \\ -w \\ \varphi \\ M \\ V \\ N \end{Bmatrix} = \begin{bmatrix} K_{i1} & \cdots & K_{i6} \\ -1 & \cdots & -1 \\ r_{i1} & \cdots & r_{i6} \\ \dfrac{D}{R_n^2}(-r_{i1}^2 + K_{i1} r_{i1}) \mathrm{e}^{\pi r_{i1}} & \cdots & \dfrac{D}{R_n^2}(-r_{i6}^2 + K_{i6} r_{i6}) \mathrm{e}^{\pi r_{i6}} \\ \dfrac{D}{R_n^3}(-r_{i1}^3 + K_{i1} r_{i1}^2) \mathrm{e}^{\pi r_{i1}} & \cdots & \dfrac{D}{R_n^3}(-r_{i6}^3 + K_{i6} r_{i6}^2) \mathrm{e}^{\pi r_{i6}} \\ \dfrac{D}{R_n^3}(1 + K_{i1} r_{i1}^2) \mathrm{e}^{\pi r_{i1}} & \cdots & \dfrac{D}{R_n^3}(1 + K_{i6} r_{i6}) \mathrm{e}^{\pi r_{i6}} \end{bmatrix} \begin{Bmatrix} C_{i1} \\ C_{i2} \\ C_{i3} \\ C_{i4} \\ C_{i5} \\ C_{i6} \end{Bmatrix} = [B_i]\{C_i\}. \tag{20}$$

To determine the transfer matrix for an individual C-block, the equations of motion are used to derive expressions for each of the state variables. The transfer matrix for a system is [28]

$$[U_i] = [B_i]|_{\pi} \, [B_i]^{-1}|_0, \tag{21}$$

where for the C-block, $[B_i]$ is the matrix of solutions defined in equation (20).

2.2.2. *Derivation of transfer matrix for a serial C-block*

The serial C-block is constructed from a series of identical C-blocks, having the same transfer matrix, joined at their boundaries. Because of the alternate orientation of the C-blocks, state variables between adjacent C-blocks are not automatically matched, as seen in the boundary conditions of equation (14). Thus, in addition to the transfer matrix for an individual C-block, a co-ordinate transformation matrix $[L]$, must be derived to satisfy the boundary conditions between adjacent C-blocks (equation (14)). Between the kth and $(k+1)$th C-block, this relation is

$$\{z_i\}_{k+1}|_0 = [L]\{z_i\}_k|_\pi. \tag{22}$$

An inspection of the boundary conditions of equation (14) shows that, at the boundary between adjacent C-blocks, the circumferential displacement and normal force are in the same direction, while the radial displacement, slope, moment, and shear alter their direction due to the change in local coordinates. Thus

$$[L] = \begin{bmatrix} 1 & 0 & 0 & 0 & 0 & 0 \\ 0 & -1 & 0 & 0 & 0 & 0 \\ 0 & 0 & -1 & 0 & 0 & 0 \\ 0 & 0 & 0 & -1 & 0 & 0 \\ 0 & 0 & 0 & 0 & -1 & 0 \\ 0 & 0 & 0 & 0 & 0 & 1 \end{bmatrix}. \tag{23}$$

Since the serial C-block actuator is comprised of n individual C-blocks that are connected at their boundaries, the transfer matrix equation for the serial C-block is n C-block transfer matrices (equation (21)) combined with $(n-1)$ co-ordinate transformation matrices (equation (23)):

$$\{z_i\}_n|_\pi = [U_i]([L][U_i])^{n-1}\{z_i\}_0|_0 = [U_i]_n\{z_i\}_0|_0. \tag{24}$$

The boundary conditions of the serial C-block (equations (12) and (13)) require the state variables at the boundaries to be

$$\{z_i\}_n|_\pi = \{u \quad -w \quad \varphi \quad 0 \quad 0 \quad 0\}^{\mathrm{T}} \quad \text{and} \quad \{z_i\}_0|_0 = \{0 \quad 0 \quad 0 \quad M \quad V \quad N\}^{\mathrm{T}}. \tag{25}$$

The real power of the transfer matrix method is in the simplification of the system of equations needed to develop the model for the behavior of the C-block. For a series of n C-blocks, Hamilton's method produced n sets of equations of motion (equation (10)) and a set of $6n$ total boundary conditions (equations (12)–(14)). All of this information, however, was collapsed into a 6×6 matrix equation (24) with two vector boundary conditions (25) using the transfer matrix method. Since the matrix equation consists of a multiplication of repeated basic elements, the difficulty of obtaining a solution with increasing n, rather than increasing geometrically, remains unchanged. This advantage of the transfer matrix method is exploited to determine the dynamic behavior of the generic serial C-block.

2.3. DYNAMIC FREQUENCY–AMPLITUDE MODEL DERIVATION

The application of the transfer matrices to the dynamic frequency–amplitude model derivation is divided into two parts. Initially, the transfer matrices are formed into an eigenvalue problem to find the undamped natural frequencies and associated modeshapes. These undamped frequencies and modeshapes, along with the original equations of motion,

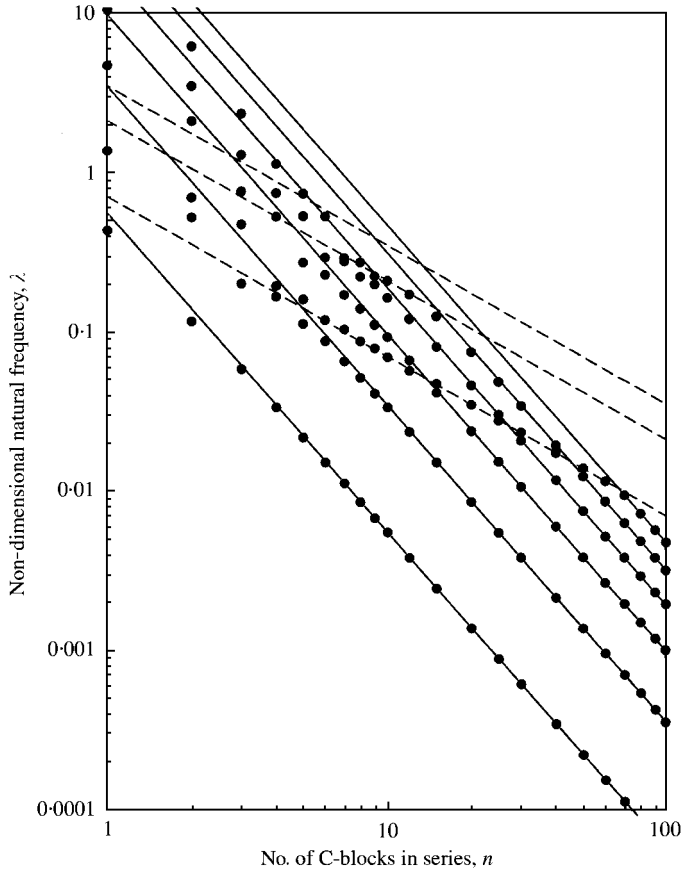

Figure 4. Non-dimensional natural frequencies for serial C-blocks. The first six non-dimensional natural frequencies, $\lambda_i^2 = \rho\omega_i^2 R_n^4/D$, for a serial C-block, and the bending and extensional frequencies of a dynamically equivalent straight bender, λ_{eq}, are given as a function of number of C-blocks in series, n: ●, serial C-block natural frequency; ——, equivalent bending natural frequency; – – – – –, equivalent extensional natural frequency.

are then used in a modal analysis procedure to determine the damped amplitude response at any forcing frequency.

2.3.1. *Natural frequencies*

The natural frequencies are obtained by examining the serial transfer matrix (24). For the equality of equation (24) to hold, the lower right quadrant of the serial transfer matrix $[U_i]_n$, must be singular. The values of the non-dimensional natural frequency, λ_i, that satisfy this singularity condition are the non-dimensional natural frequencies of the C-block series. These values are given in Figure 4 for series of C-blocks ranging from 1 to 100. This figure shows that, as the number of C-blocks in series increases, the natural frequencies monotonically decrease. It is interesting to note that, for lower modes and higher numbers in series (above 10), the natural frequency locations approach and straight lines on the log–log graph of Figure 4. These straight lines represent the natural frequencies of an equivalent straight bender, with bending natural frequencies being

represented by solid lines and extensional natural frequencies being represented by dashed lines. The equivalent straight bender is discussed in more detail in section 2.4.

2.3.2. *Serial C-block mode shapes*

The transfer matrix procedure can also be used to determine the mode shapes associated with each natural frequency by eliminating one of the dependent equations from the singular transfer matrix (24). Since the mode shapes have no absolute magnitude, any one of the non-zero boundary state variables can be set to an arbitrary value, resulting in an inhomogeneous 5×5 matrix equation. In this case it is convenient to set the series radial tip deflection to one, i.e., $w_n|\pi = 1$, since, because of the construction of serial C-block, this deflection is guaranteed not to be zero. This condition is substituted into equation (24), which is reduced, rearranged, and solved to determine the remainder of the state variables. Thus, the relative sizes of all boundary state variables are known.

To find the complete modeshape, the values of the deflection state variables, u and w, must be known at all points. Since the boundary state vector $\{z_i\}_0|_0$ is known, the state variables at the endpoints of the kth C-block are calculated from the equation

$$\{z_i\}_k|_0 = ([L][U_i])^{k-1} \{z_i\}_0|_0 . \tag{26}$$

The state variables at any point in the kth C-block in the series is determined as [28]

$$\{z_i\}_k = [B_i][B_i]^{-1}|_0 \ \{z_i\}_k|_0 , \tag{27}$$

where $[B_i]$ is given in equation (20).

Combining equations (26) and (27) gives the state variables at any point in the kth C-block in the series as

$$\{z_i\}_k = [B_i][B_i]^{-1}|_0 ([L][U_i])^{k-1} \{z_i\}_0|_0 . \tag{28}$$

Thus, since the displacements u and $-w$ are the first two state variables, the modeshapes for the kth C-block actuator are the first two rows of equation (28), with the second row being negative. The modeshape for the entire serial C-block array is the piecewise sum of each of the n individual modeshapes (equation (28)) that are defined over the kth C-block.

2.3.3. *Modal analysis*

To derive the full dynamic model for the C-block, the mode shapes and natural frequencies are used in a modal analysis technique to determine the response of the C-block due to the internal piezoelectric forcing functions. These forcing functions are assumed to be sinusoidal in time with a forcing frequency of Ω.

To calculate the frequency–amplitude relationship, the forced displacements are assumed to be the sum of a series of orthogonal, homogeneous solutions, u_{hi} and w_{hi}, and particular solutions $U_p(\theta)$ and $W_p(\theta)$,

$$\begin{Bmatrix} u \\ w \end{Bmatrix}_k = \begin{Bmatrix} U_p(\theta) \\ W_p(\theta) \end{Bmatrix}_k \sin \Omega t + \sum_{i=1}^{\infty} \begin{Bmatrix} u_{hi} \\ w_{hi} \end{Bmatrix}_k \alpha_i(t). \tag{29}$$

A convenient set of homogeneous solutions is the mode shapes associated with each undamped natural frequency (equation (28)), and a convenient particular solution is the static solution. The full form of the static solution is calculated in much the same way as the dynamic mode shapes, but using a simplified static transfer matrix where dynamic terms are

eliminated. The static solution mode shape resulting from an internal piezoelectric moment forcing is

$$\begin{Bmatrix} U_p(\theta) \\ W_p(\theta) \end{Bmatrix}_k = \begin{bmatrix} 2k-1 & \frac{-\pi}{2}\,[(-1)^k(2k-1)+1] \\ \frac{-\pi}{2}[(-1)^k(2k-1)+1] & -(2k-1) \\ -1 & 0 \\ \frac{-\pi}{2}\,[(-1)^k+1] & 1 \end{bmatrix}^T \begin{Bmatrix} \sin\theta \\ \cos\theta \\ \theta \\ 1 \end{Bmatrix} \frac{M^P R_n^2}{D}. \tag{30}$$

It is interesting to note that the reorientation of the local co-ordinate system that requires the inclusion of the co-ordinate transformation matrix $[L]$, (equation (23)) also alters the sign of some terms of equation (30), as seen by the inclusion of the $(-1)^k$ factor.

When the solution (29) is substituted into the n sets of equations of motion (10), the boundary conditions are homogenized and each set of equations of motions are simplified to

$$\lambda_i^2 \begin{Bmatrix} \sum_{i=1}^{\infty} u_{hi}\,\alpha_i(t) \\ \sum_{i=1}^{\infty} w_{hi}\,\alpha_i(t) \end{Bmatrix}_k + \frac{\gamma}{\Omega}\lambda_i^2 \begin{Bmatrix} \sum_{i=1}^{\infty} u_{hi}\,\alpha_i(t)_{,t} \\ \sum_{i=1}^{\infty} w_{hi}\,\alpha_i(t)_{,t} \end{Bmatrix}_k + \frac{\Lambda^2}{\Omega^2} \begin{Bmatrix} \sum_{i=1}^{\infty} u_{hi}\,\alpha_i(t)_{,tt} \\ \sum_{i=1}^{\infty} w_{hi}\,\alpha_i(t)_{,tt} \end{Bmatrix}_k = \Lambda^2 \begin{Bmatrix} U_p(\theta) \\ U_p(\theta) \end{Bmatrix}_k \sin\Omega t. \tag{31}$$

This set of second order ordinary differential equations holds for each of the n C-blocks in the series. When all n sets of equations of motion (31) are added together, the sum is

$$\lambda_i^2 \sum_{k=1}^{n} \begin{Bmatrix} \sum_{i=1}^{\infty} u_{hi}\,\alpha_i(t) \\ \sum_{i=1}^{\infty} w_{hi}\,\alpha_i(t) \end{Bmatrix}_k + \frac{\gamma}{\Omega}\lambda_i^2 \sum_{k=1}^{n} \begin{Bmatrix} \sum_{i=1}^{\infty} u_{hi}\,\alpha_i(t)_{,t} \\ \sum_{i=1}^{\infty} w_{hi}\,\alpha_i(t)_{,t} \end{Bmatrix}_k + \frac{\Lambda^2}{\Omega^2} \sum_{k=1}^{n} \begin{Bmatrix} \sum_{i=1}^{\infty} u_{hi}\,\alpha_i(t)_{,tt} \\ \sum_{i=1}^{\infty} w_{hi}\,\alpha_i(t)_{,tt} \end{Bmatrix}_k$$

$$= \Lambda^2 \sum_{k=1}^{n} \begin{Bmatrix} U_p(\theta) \\ U_p(\theta) \end{Bmatrix}_k \sin\Omega t. \tag{32}$$

This form is used to simplify the equations and determine the final dynamic model.

2.3.4. *Solution to equations of motion*

The only unknown quantity in these equations (31) and (32) is the form of the time function, $\alpha_i(t)$ multiplying each modeshape, which is independent of the C-block index, k. To determine the time function $\alpha_i(t)$, the orthogonality relation involving the modeshapes is exploited, setting all terms but one in the summation to zero, resulting in

$$\lambda_i^2\,\alpha_i(t) + \frac{\gamma}{\Omega}\,\lambda_i^2\alpha_i(t)_{,t} + \frac{\Lambda^2}{\Omega^2}\,\alpha_i(t)_{,tt} = \Lambda^2\beta\sin\Omega t, \tag{33}$$

where

$$\beta = \frac{\sum_{k=1}^{n} \left[\int_0^{\pi} \{U_p(\theta)\, W_p(\theta)\}_k \cdot \{u_{hi}\, w_{hi}\}_k^{\mathrm{T}}\, \mathrm{d}\theta \right]}{\sum_{k=1}^{n} \left[\int_0^{\pi} \{u_{hi}\, w_{hi}\}_k \cdot \{u_{hi}\, w_{hi}\}_k^{\mathrm{T}}\, \mathrm{d}\theta \right]}. \tag{34}$$

Equation (33) is a forced, second order ordinary differential equation. Although the transient response can be calculated, the steady state response is of most interest in this derivation, so only the particular solution for the governing differential equation (33) is required. The particular solution to equation (33) is

$$\begin{aligned} \alpha_i(t) &= \frac{\Lambda^2 \beta}{\sqrt{(\lambda_i^2 - \Lambda^2)^2 + (\gamma\lambda_i^2)^2}} \sin\left(\Omega t - \tan^{-1} \frac{\gamma\lambda_i^2}{\lambda_i^2 - \Lambda^2}\right) \\ &= \frac{\Lambda^2 \beta}{((\lambda_i^2 - \Lambda^2)^2 + (\gamma\lambda_i^2)^2)} \left[(\lambda_i^2 - \Lambda^2)\sin(\Omega t) + \gamma\lambda_i^2 \cos(\Omega t)\right]. \end{aligned} \tag{35}$$

2.3.5. *Frequency–amplitude model*

For actuation purposes, the C-block is connected to the rest of the system at its tip ($k = n$, $\theta = \pi$). For this case, the magnitude of the resulting frequency–amplitude model in the radial direction is

$$w_n = \frac{M^P R_n^2}{D} \sqrt{\left\{2n - \sum_{i=1}^{\infty} \frac{\Lambda^2 W_i(\lambda_i^2 - \Lambda^2)}{[(\lambda_i^2 - \Lambda^2)^2 + (\gamma\lambda_i^2)^2]}\right\}^2 + \left\{\sum_{i=1}^{\infty} \frac{\Lambda^2 W_i(\gamma\lambda_i^2)}{[(\lambda_i^2 - \Lambda^2)^2 + (\gamma\lambda_i^2)^2]}\right\}^2} \tag{36}$$

and, in the circumferential direction,

$$u_n = (-1)^n \frac{M^P R_n^2}{D} \sqrt{\left\{\pi n + \sum_{i=1} \frac{\Lambda^2 U_i(\lambda_i^2 - \Lambda^2)}{[(\lambda_i^2 - \Lambda^2)^2 + (\gamma\lambda_i^2)^2]}\right\}^2 + \left\{\sum_{i=1}^{\infty} \frac{\Lambda^2 U_i(\gamma\lambda_i^2)}{[(\lambda_i^2 - \Lambda^2)^2 + (\gamma\lambda_i^2)^2]}\right\}^2}. \tag{37}$$

These two equations represent the behavior of the tip of a serial C-block. In addition, because of the identical equations of motion, these equations represent the behavior of any series within an array structure, and, by extension, the motion of the entire array.

The values of the longitudinal orthogonality constants, W_i, and transverse orthogonality constants, U_i, are calculated by solving the equations above, and are given in Figures 5 and 6 for series of C-blocks ranging from 1 to 100. These figures show that some of the orthogonality constants tend to approach the straight lines on the graph; this behavior is most apparent for the transverse constants (Figure 6) of larger magnitude. The straight lines represent the orthogonality constants of an equivalent straight bender, which is discussed in more detail in the following section.

2.4. DYNAMICALLY EQUIVALENT STRAIGHT BENDER

The dynamic behavior of large numbers of C-blocks in series show some interesting trends. As the number of C-blocks is increased, the behavior of the serial C-block approaches the behavior of a dynamically equivalent straight bender. The dynamic behavior of a straight bender is much easier to calculate; thus, this approximation is very

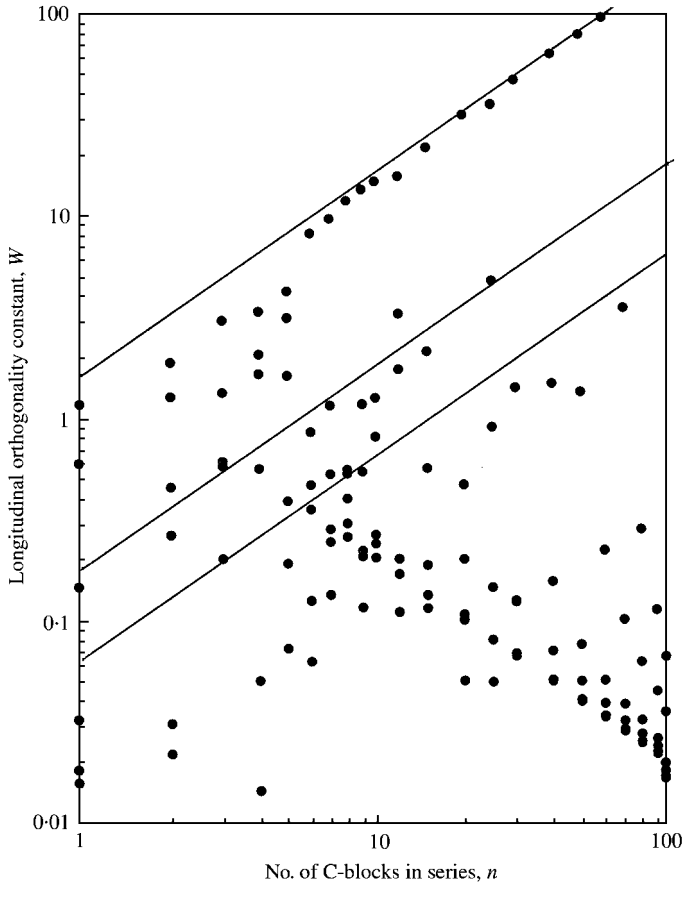

Figure 5. Longitudinal orthogonality constants for serial C-blocks. The longitudinal orthogonality constants, W_i, are given for a serial C-block and a dynamically equivalent straight bender as a function of number of C-blocks in series, n: ●, serial C-block W; ———, equivalent straight rod.

useful for designing long series of C-blocks. The straight bender has overall macroscopic parameters such that its transverse, beam-like properties and longitudinal, rod-like properties are the same as the serial C-block; i.e., the length, mass, longitudinal stiffness, and rotational stiffness match.

In this section, the behavior of a dynamically equivalent straight bender is determined. The macroscopic parameters of the straight bender are calculated as a function of the C-block parameters. The natural frequencies and orthogonality constants of the straight bender are then calculated using standard methods, and these values are calculated as a function of the parameters of the C-block array. The natural frequencies and orthogonality constants of the C-block and the equivalent straight bender are compared, and the accuracy of this comparison is discussed.

2.4.1. *Equivalent parameters*

The length of the dynamically equivalent straight bender must match that of the serial C-block. This is accomplished by requiring that

$$L_{eq} = 2nR_n. \tag{38}$$

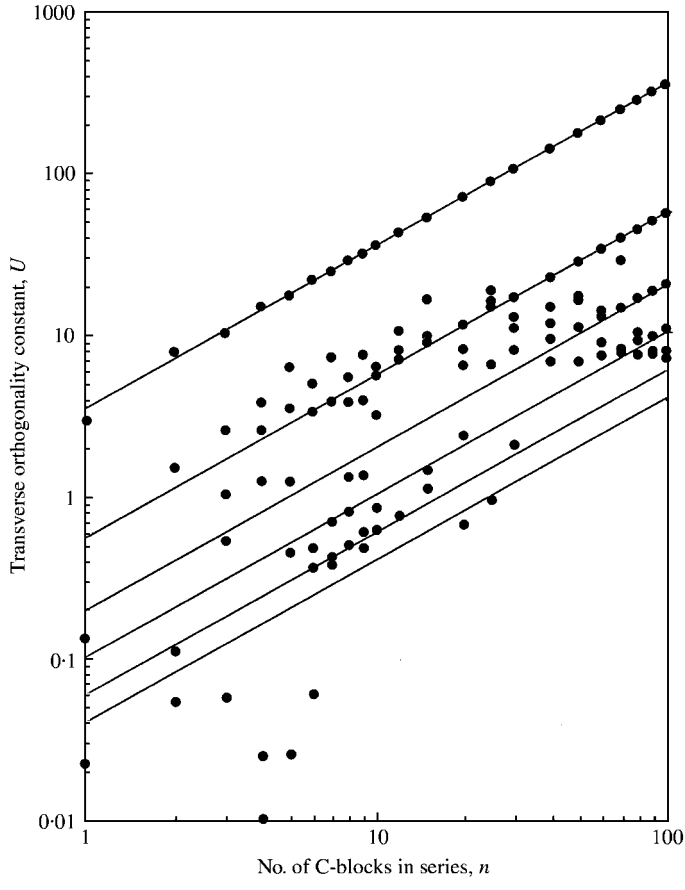

Figure 6. Transverse orthogonality constants for serial C-blocks. The circumferential orthogonality constants, U_i, are given for a serial C-block and a dynamically equivalent straight bender as a function of number of C-blocks in series, n: •, serial C-block U; ——, equivalent straight bender.

The total mass of the serial C-block is $\rho n \pi R_n$. The total mass of the equivalent straight bender is $\rho_{eq} L_{eq}$. Equating the two masses and using the length definition (38) requires that the mass per unit length of the equivalent straight bender, ρ_{eq}, be

$$\rho_{eq} = \frac{\pi}{2} \rho. \tag{39}$$

The stiffnesses of the serial C-block are calculated using Castigliano's theorem. Equating the stiffnesses of the serial C-block and the straight bender and substituting the length of the dynamically equivalent straight bender (38) results in an expression for the equivalent extensional stiffness, A_{eq}, of

$$A_{eq} = 4D/(\pi R_n^2) \tag{40}$$

and an expression for the equivalent bending stiffness, D_{eq}, of

$$D_{eq} = 2D/\pi. \tag{41}$$

Using these expressions for length, mass per length, and stiffness, the bending and extensional motion of the dynamically equivalent straight bender are calculated using

TABLE 1

Natural frequencies and orthogonality constants of a straight beam and a straight rod. The bending and extensional non-dimensional natural frequencies and orthogonality constants for an equivalent straight beam are given with no tip mass

Mode	Param.	1	2	3	4	5	6
Bending	λ_{beq}	3·516	22·024	61·68	120·89	199·65	298·6
	U_{eq}	3·574	− 0·5707	0·2029	− 0·1040	0·06092	− 0·0412
Extension	λ_{eeq}	1·571	4·712	7·853			
	W_{eq}	1·6211	0·1801	0·06434			

standard methods [25]. From this analysis, the non-dimensional natural frequencies, λ_{beq} and λ_{eeq}, and orthogonality constants, U_{eq} and W_{eq}, for the bending and extensional motions of the equivalent straight bender are determined. Values for these parameters are given in Table 1.

The non-dimensional natural frequencies for the equivalent straight bender, λ_{beq} and λ_{eeq}, cannot be used directly in the dynamic C-block model (equations (32) and (33)) in place of the non-dimensional C-block frequency, λ_i, because the C-block frequency (equation (15)) has a different relationship to ω_i. The equivalent straight bender frequencies, λ_{beq} and λ_{eeq}, depend on the length (38) and stiffness (40) of the dynamically equivalent straight bender rather than the C-block radius, R_n, and stiffness, D. Thus, an equivalent approximate frequency, λ_{eq}, is defined as a function of λ_{beq} and λ_{eeq}. The bending natural frequencies of the equivalent straight beam are

$$\lambda_{eq} = \lambda_{beq}/(2n^2\pi), \tag{42}$$

where values for λ_{beq} are given in Table 1. Likewise, the extensional natural frequencies of the equivalent straight beam are

$$\lambda_{eq} = \sqrt{2}\lambda_{eeq}/(n\pi), \tag{43}$$

where values for λ_{eeq} and corresponding orthogonality constants are given in Table 1. The bending natural frequencies (equation (42)) are used along with the bending orthogonality constant, U_{eq}, in the transverse C-block model (equation (37)), while the extensional natural frequencies (equation (43)) are used along with the extensional orthogonality constant, W_{eq} in the longitudinal C-block model (equation (36)).

2.4.2. *Discussion of equivalent straight bender*

The non-dimensional natural frequencies and orthogonality constants for the equivalent straight bender are included as straight lines on the graphs of serial C-block non-dimensional natural frequencies and orthogonality constants (Figures 4–6). Both bending and extensional natural frequencies are included on the natural frequency graphs; the bending and extensional orthogonality constants for each mode are included on the appropriate charts of U_i and W_i. These figures show that, as the number of C-blocks in the series increases, the frequencies and orthogonality constants look more and more like that of an equivalent straight bender. Interestingly, the serial C-block reproduces both the bending, beam-like behavior and the extensional, rod-like behavior of the equivalent bender.

In the natural frequency chart (Figure 4), the natural frequencies of the C-block are somewhat scattered at low numbers in series (less than approximately 10). However, as the number of C-blocks in series gets larger (above 10) and the serial C-block gets longer, the natural frequencies rapidly approach the natural frequencies of the equivalent straight bender. This is particularly apparent above about 10 in series, where the C-block frequencies are very close to the straight bender. It is also interesting to note that the C-block natural frequencies match both bending and extensional natural frequencies of the straight bender.

This asymptotic behavior is also apparent in the orthogonality constant graphs. However, because the natural frequencies of the C-block tend to be associated with either extension or bending, the orthogonality constants tend to coverage to the straight bender only for modes where the motion of the C-block matches the motion of the bender. For example, in Figure 5, the extensional orthogonality constants, W_i, tend to approach the extensional orthogonality constants of the equivalent straight rod, but only for those modes that are primarily extensional. The remainder of the extensional orthogonality constants, those corresponding to modes having primarily a bending behavior, tend to decrease as the extensional and bending behavior of the C-block becomes more uncoupled, resulting in a scattering of data points. In Figure 6, the bending orthogonality constants, U_i, tend to approach the bending orthogonality constants of the equivalent straight beam, but only at natural frequencies that are primarily bending. Since the lower modes of long C-blocks are primarily bending, the asymptotic behavior is more pronounced in Figure 6 than in Figure 5.

The alignment of the natural frequencies with the predicted extensional and bending natural frequencies (Figure 4) gives an indication of the behavior of the C-block array. In particular, as the number of C-blocks in series increases, the bending and extensional modes become increasingly uncoupled. For example, for a large number of C-blocks in series (over 70), the first six modes calculated are all primarily bending modes. Thus, the bending orthogonality constants in Figure 6 align closely with the predicted bending constants for large numbers in series , while, in Figure 5, the orthogonality constants for the same modes are nowhere near the predicted extensional orthogonality constants due to the minimal extensional behavior of these modes. For all these figures, as the number of C-blocks in series increases, the straight beam approximation becomes better due to the uncoupling of the bending and extensional modes of the serial C-block.

2.4.3. *Accuracy of approximation*

The first non-dimensional natural frequency of the C-block is quite well approximated by the equivalent straight bender frequencies even at lower numbers in series. For example, Table 2 gives the minimum number of C-blocks in series required for the straight bender frequency approximation to match within 5, 1, and 0·1% are given as a function of the mode number. For numbers in series above 10, the minimum number in series required is rounded upwards to 12, 15, 20, 25, 30, 40, 50, 60, 80, or 100 C-blocks in series, since these were the configurations specifically examined. For the first natural frequency, which is of most interest in design, the equivalent straight bender approximation is accurate to within 5% for only four C-blocks in series, and accurate to within 1% for only eight C-blocks in series.

Natural frequencies associated with higher modes are less accurately approximated by the straight bender. This is due to the more complex modeshapes of the higher frequencies, where the straight bender approximation does not match as well. However, even the first four modes are approximated to within 5% by as few as 10 C-blocks in series. The orthogonality constants are predicted less well by the straight bender due to the differences

TABLE 2

Accuracy of dynamically equivalent straight bender approximation for natural frequencies and orthogonality constants. The minimum number of C-block in series required for the dynamically equivalent straight bender approximation to match the natural frequency and orthogonality constants of the serial C-block to within accuracies of 5, 1 *and* 0·1% *are given as a function of the mode number. For numbers above* 10, *the minimum number is rounded upwards to* 12, 15, 20, 25, 30, 40, 50, 60, 80, *or* 100 *C-blocks in series*

Quantity	Accuracy X%	Minimum # C-blocks in series, n, required for X% accuracy					
		Mode 1	Mode 2	Mode 3	Mode 4	Mode 5	Mode 6
Natural frequency λ_i	5	4	9	6	10	12	20
	1	8	20	30	40	25	40
	0·1	30	60	80	100	> 100	> 100
Orthogonality constants W_i, U_i	5	5	30	70	> 100	> 100	> 100
	1	12	30	> 100	> 100	> 100	> 100
	0·1	40	80	> 100	> 100	> 100	> 100

between modeshapes; however, the prediction is good for lower modes. In fact, for the first natural frequency, the equivalent straight bender approximation is accurate to within 5% for only five C-blocks in series, and accurate to within 1% for only 12 C-blocks in series.

The straight bender approximation is significant because it demonstrates that the complex serial array of C-blocks, having $2n$ equations of motion, can be accurately modelled by a straight bender having only two equations of motion. Moreover, the more individual C-blocks contained in the serial C-block, the more accurate the approximation. Although this approximation breaks down for only a few C-blocks in series, necessitating the use of the more complex exact model, the approximation is surprisingly accurate for longer series of C-blocks. Thus, paradoxically, the more complex the exact model, the more accurate the simple approximation.

3. EXPERIMENTAL VALIDATION

To experimentally verify the radial frequency–amplitude model (equation (36)), a number of prototypes were fabricated and the tip amplitudes were experimentally recorded through a range of input frequencies. The prototypes were constructed with a low number in series so that the more complex portion of the analytical model, where the straight bender approximation is not yet accurate, could be tested. Two different piezoelectric materials were used to fabricate these prototypes: polyvinylidene fluoride (PVdF) polymeric material and PZT 5-H ceramic material. The fabrication procedures, test procedures and results from two example prototypes from each material are presented below.

3.1. PROTOTYPE FABRICATION

Prototypes from each material were fabricated using off-the-shelf materials and bench-top techniques. The two materials used had widely different stiffness and piezoelectric properties (Figure 7), allowing the model to be verified across a wide non-dimensional space. The ceramic PZT material was chosen because ceramics are used in

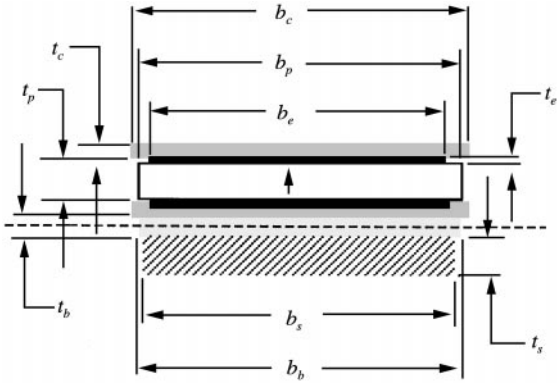

Figure 7. Unimorph C-block cross-section. The unimorph C-block cross-section consists of a piezoelectric layer bonded to a substrate. Additional layers include electrode layers and coating layers. The subscripts *p*, *s*, *b*, *e*, and *c* refer to the piezoelectric, substrate, bonding, electrode, and coating layers, respectively: □, piezoelectric layers, PZT-5H ($Y = 63$ GPa) or PVdF ($Y = 5{\cdot}4$ GPa); □, epoxy layer ($Y = 1{\cdot}90$ GPa); ■, Electrode non-existant or silver paste ($Y = 0{\cdot}70$ GPa); ▨, substrate, steel ($Y = 194$ GPa) or aluminum ($Y = 65$ GPa); ■, coating: non-existant or polymer ($Y = 1{\cdot}00$ GPa); ↑ poling direction.

smart structures applications requiring high-energy density, and PZT-5H has a relatively high piezoelectric constant, d_{31}, and thus could be run to higher displacements with lower input voltage. The PVdF polymeric material was chosen because it presents a substantial contrast in material properties when compared to the ceramic materials. Because the polymer is supplied in a thin film form, this material is also inexpensive and easy to use to fabricate prototypes. All prototypes were constructed as unimorphs (Figure 7) to simplify fabrication and avoid potential problems associated with matching diameters of two different piezoceramic materials.

3.1.1. *PZT-5H ceramic prototypes*

To construct the ceramic actuators, commercially available circular half-tubes of PZT-5H with preplated electrodes were procured from Morgan Matroc Electroceramics. The half-tubes were 10·0 mm in outside radius and 0·838 mm in thickness, with a width of approximately 12·2 mm. The thickness of the electrode layer was only 2–5 μm, which is significantly less than the other layers; therefore, this layer was neglected in calculating the physical constants of the C-block. The piezoelectric constant of the PZT-5H was measured in the lab by directly measuring the displacement of a sample as a function of voltage. The resultant piezoelectric constant, 380 pm/V, was substantially higher than the published value for this material.

To fabricate substrates to match the ceramic half-tubes, strips of 0·455 mm stainless steel were cut to 12·2 mm in width to match the ceramic. These strips of steel were bent around a double mandrel into a recursive S-shape as shown in Figure 8(a). The mandrel was sized so that the outside radius of the resulting substrate was 9·16 mm, and thus conformed to the inner diameter of the ceramic.

Once the steel was bent, the substrate was cleaned and roughened to improve the adhesion of the epoxy. The ceramic was then epoxied to the steel with a layer of Insulcast 501 epoxy approximately 100 μm thick. After the epoxy cured, lead wires were soldered in between adjacent ceramics. In addition, a lead wire was soldered to the base of the C-block to connect to the power supply. A completed ceramic prototype is shown in Figure 8(b). The dimensions of these prototypes are given as prototypes 1 and 2 in Table 3.

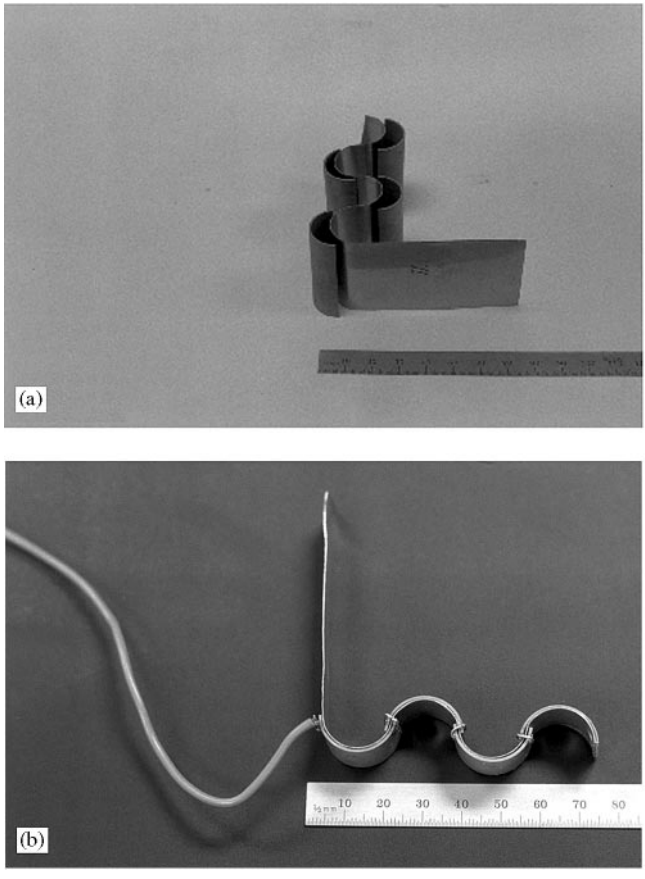

Figure 8. Ceramic C-block prototype fabrication. Two prototypes were fabricated to test the prototype arrays. (a) A steel substrate was bent to conform to the inner radius of ceramic semicircles. (b) Two prototypes were constructed, one with two in series and one with four in series. These prototypes are shown with the tip mass used for dynamic testing attached.

TABLE 3

C-block array experimental prototype geometric parameters. Two prototypes were constructed for performance testing. This table gives the outer radii, widths, and thicknesses for these prototypes. Parameters given include the radius, the width and thickness of each layer, and the stiffness ratio. The subscripts p, e, b, s, and c represent the piezoelectric, electrode, bonding, substrate, and coating layers respectively

Proto no.	No. in series	Piezo material	Outer radius (mm)	Thickness (μm)					Width (mm)				
				t_p	t_c	t_e	t_b	t_s	b_p	b_c	b_e	b_b	b_s
1	2	PZT-5H	10·0	838	—	—	76	455	12·2	—	—	12·2	12·2
2	4	PZT-5H	10·0	838	—	—	122	455	12·2	—	—	12·2	12·2
3	2	PVdF	9·5	52	12	6·5	25	25	22·2	22·2	18·8	18·5	18·5
4	3	PVdF	7·8	52	12	6·5	25	25	22·2	22·2	18·8	18·5	18·5

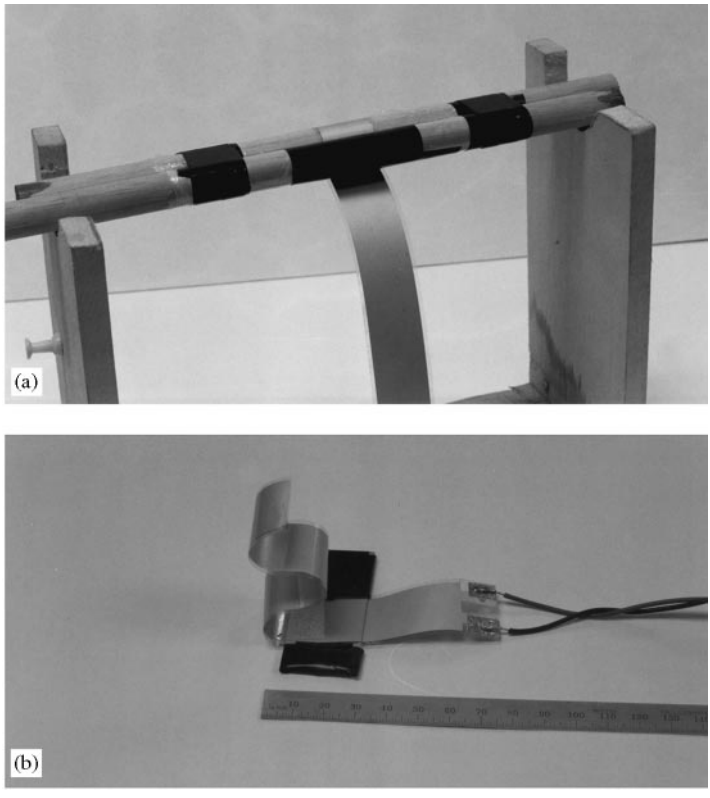

Figure 9. Ceramic C-block prototype fabrication. The polymeric serial C-block actuators were fabricated from PVdF piezoelectric film. (a) The PVdF film was bonded to aluminum foil or to another layer of film and wrapped around a dowel fixture. (b) After the epoxy cured, the prototypes were clamped between glass slides and connected to electrodes to form the final prototype.

3.1.2. *PVdF polymeric prototypes*

Polymeric prototypes were fabricated from commercially procured PVdF film manufactured by AMP Incorporated. The film was 22·2 mm wide and 52 μm thick, and was pre-electroded with a 6·4 μm thick silver electrode which was covered with a protective coating of 12 μm thick. The film was epoxied to alternating 18·5 mm wide, 25 μm thick aluminium substrates using a 25 μm thick layer of Insulcast 501 epoxy manufactured by Permagile Industries. The substrate was bonded to alternating sides of the film to change the sign of the bending moment in adjacent C-blocks. The bonded film was wrapped around dowels in alternating directions as shown in Figure 9(a) and the epoxy was allowed to cure. The film was then removed from the dowels and electrodes were attached to form the final prototypes using conductive tape. A completed polymeric prototype is shown in Figure 9(b). The dimensions of these prototypes are given as prototypes 3 and 4 in Table 3.

3.2. TEST SET-UP AND PROCEDURE

The dynamic testing method was slightly different between the ceramic and polymeric prototypes. For all prototypes, the C-block was clamped in place and connected to a variable frequency source, and a Philtec model A88NE1 fiber optic probe was used to

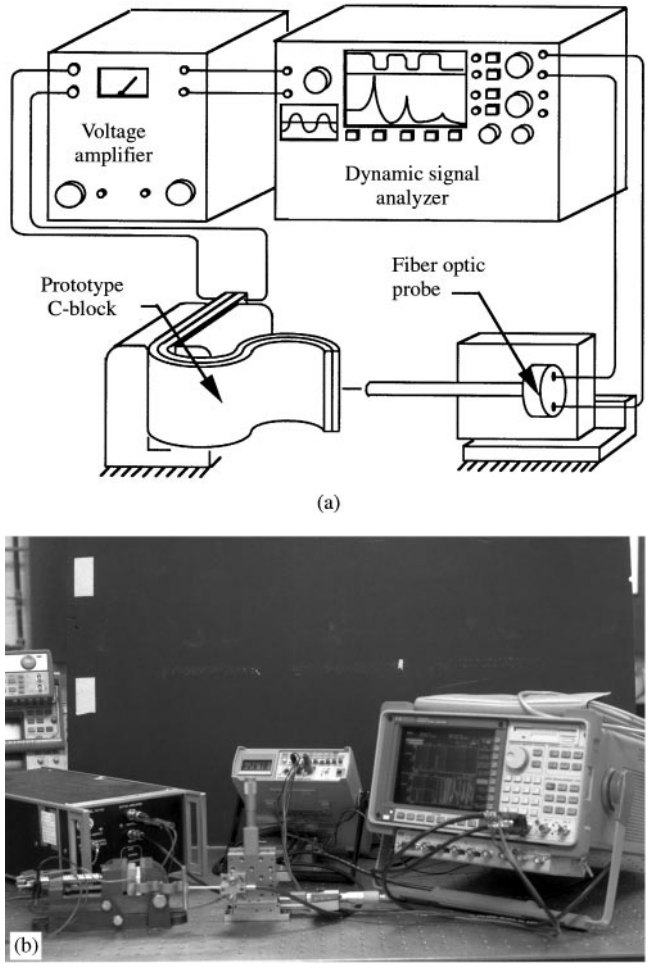

Figure 10. Frequency–amplitude experimental apparatus. The amplitude output of the C-block arrays as a function of frequency input was measured with a fiber optic probe connected to a dynamic signal analyzer. (a) The diagram of the test set-up shows all pieces of equipment. (b) Photograph of test set-up.

track the position of the tip of the C-block and the phase of the displacement. For each ceramic prototype, the input to the C-block and the output from the fiber optic probe was connected to an HP model 35670A dynamic frequency analyzer, as shown in Figure 10. For each polymeric prototype, the C-block connected to an HP 33120A frequency generator and the fiber optic probe was connected to an HP 54601B oscilloscope.

To perform the experiment, an 5 V input sine wave was applied to each C-block from the dynamic signal analyzer. The frequency of this sine wave was swept from a minimum frequency below the first resonant frequency to a maximum in thousands of Hertz. These minimum and maximum frequencies varied from prototype to prototype to ensure that the lowest natural six frequencies were captured. At intermediate frequencies, the peak amplitude and phase of the tip displacement of the C-block was measured using the dynamic signal analyzer.

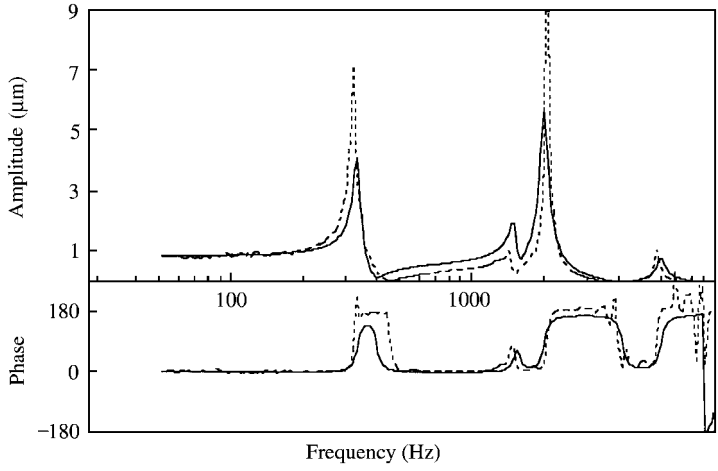

Figure 11. Frequency–amplitude experimental results for C-block array prototype 1. These results are for a ceramic unimorph of two C-blocks with outside radius = 10·00 mm at 5 V input. The geometric parameters of this prototype are given as prototype 1 in Table 3, and the results and errors are given in Table 4: ——, theoretical amplitude and phase; – – – – –, experimental amplitude and phase.

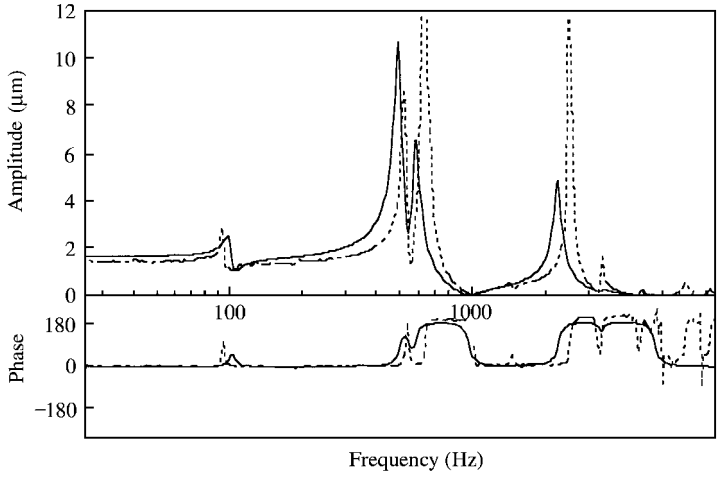

Figure 12. Frequency–Amplitude experimental results for C-block array prototype 2. These results are for a ceramic unimorph of four C-blocks with outside radius = 10·00 mm at 5 V input. The geometric parameters of this prototype are given as prototype 2 in Table 3, and the results and error are given in Table 4: ——, theoretical amplitude and phase; – – – – –, experimental amplitude and phase.

3.3. TEST RESULTS

Graphs of the experimental results for all prototypes are shown in Figures 11–14 along with the analytically predicted results. The experimentally determined locations of all natural frequencies are given in Table 4. The damping coefficients used in the analytical model were determined previously for these materials [24]. In some figures, the amplitude of the largest peaks were trimmed to show more detail at the lower frequencies. In all figures, the amplitude curve starts at the static displacement amplitude at low frequencies, and shows a series of natural frequency peaks, but with different heights and spacing. Between natural frequencies, the amplitude decreases to near zero. The material used to

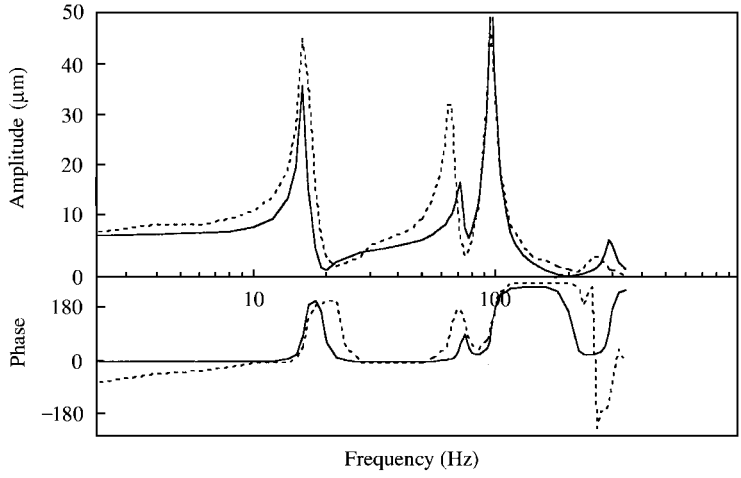

Figure 13. Frequency–amplitude experimental results for C-block array prototype 3. These results are for a ceramic unimorph of two C-blocks with outside radius = 10·00 mm at 5 V input. The geometric parameters of this prototype are given as prototype 3 in Table 3, and the results and error are given in Table 4: ——, theoretical amplitude and phase; – – – – – –, experimental amplitude and phase.

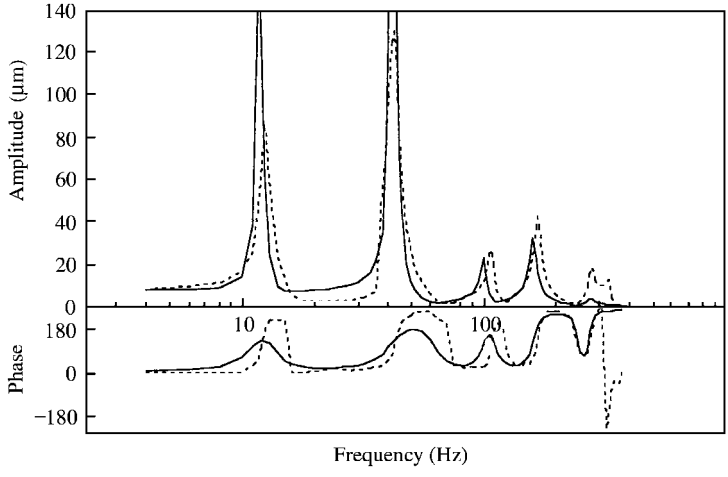

Figure 14. Frequency–amplitude experimental results for C-block array prototype 4. These results are for a ceramic unimorph of four C-blocks with outside radius = 10·00 mm at 5 V input. The geometric parameters of this prototype are given as prototype 4 in Table 3, and the results and error are given in Table 4: ——, theoretical amplitude and phase; – – – – – –, experimental amplitude and phase.

fabricate the C-blocks is underdamped, and therefore the amplitude peaks at each natural frequency are very pronounced. In Figure 12, where over six natural frequencies can be observed, only the first six are given in Table 4 to match the six derived in the model.

For all prototypes, the average difference between the predicted and measured deflection across the frequency range and the average difference between the analytical and experimental natural frequencies are given in Table 4. The correlation between the analytical model and the experimental results is very good. For the natural frequency, the average difference between the predicted and measured results ranged from 3·69 to 7·96%, with the greatest difference between the analytical and experimental values just over 12%. The

TABLE 4

C-block array frequency–amplitude experimental results. The static deflection amplitude, the experimentally determined locations of the natural frequencies, and the non-dimensional values of these frequencies are given for all prototypes. In addition, the average difference between the analytical model and the experimental results are given for the tip deflection and natural frequency locations. The percentage difference between the experimental value and analytical prediction is also given

Proto	Static amp. (μm)	Average amplitude diff. from theory to experiment		Mode	Experimental natural frequencies		
		(μm)	Percentage (%)		Location (Hz)	Non-dim. freq.	Ave. % diff. from theory to experiment
1	0·86	0·306	3·02	1	322	0·1133	− 3·24
				2	1410	0·496	− 5·71
				3	2044	0·719	2·91
				4	5761	2·027	4·46
2	1·44	0·745	3·21	1	94	0·0315	− 6·72
				2	525	0·1758	4·72
				3	644	0·216	10·31
				4	1412	0·473	− 11·16
				5	2509	0·840	12·03
				6	3400	1·138	− 0·22
3	10	4·14	8·72	1	16·3	0·118	0·67
				2	65	0·470	− 10.7
				3	96	0.694	−0.69
				4	260	1.88	− 11.39
4	8	10.56	8.13	1	12	0.0574	1.11
				2	42.5	0.203	0.20
				3	107	0·512	7·36
				4	168	0·804	4·75
				5	281	1·345	2·98
				6	525	2·512	5·75

locations of the first natural frequency, which are of most interest from a design perspective, are predicted much more accurately, to within an average of 2·93%.

For the experimentally determined amplitudes, the difference between the analytical model and experimental data averaged 0·306 and 0·745 μm for the ceramic prototypes, and 4·14 and 10.56 μm for the polymeric prototypes. This corresponds to 3·19% of the maximum experimental amplitudes for the ceramic prototypes and 8·42% for the polymeric prototypes. For the polymeric prototypes, a substantial portion of this difference is due to the imprecision of the fiber optic probe at the high amplitudes near the natural frequency locations. A substantial portion of the remainder of the error, for both polymeric and ceramic prototypes, is due to the slight inaccuracies in natural frequency location. Additionally, near the natural frequency locations, amplitude differences are likely due to inaccuracies in the damping coefficient.

The remainder of the differences between the experimental data and the analytical model, both in natural frequency location and amplitude, could easily be due to reasonable variations in the geometry of the prototypes and the experimental apparatus. The errors are likely due to variations in the bonding layer, additional compliance between adjacent

C-blocks, or compliance in the clamped end of the C-block, producing an end condition that is not perfectly fixed. Another potential source of error is associated with the higher mode shapes. These modes are more complex, and are less accurately modelled by the analytical solution. However, despite the small error, the analytical model correlates very well with experimental results.

4. PARAMETER ANALYSIS AND DISCUSSION

The experimental results, coupled with the analytical analysis, show that the C-block performance depends on two important quantities: the natural frequency locations and the amplitude of the motion. By knowing how C-block parameters form the performance models for these quantities, engineers can use the models to compare different C-block designs and optimize them to meet particular application requirements. In this section, the dependence of the natural frequency locations and the amplitude of the motion on material, geometric, and array configuration parameters is examined by performing a parameter analysis of the analytical model. To simplify the analysis, the cross-section was assumed to consist of two layers of active material of thickness a. This represents the most energy-dense and efficient construction of the C-block actuator, and allows the effect of the altering of the geometric and material parameters contained within the internal moment, M^P, and the bending stiffness, D, to be explicitly examined.

4.1. NATURAL FREQUENCY

For the first natural frequency of the C-block, the frequency location is closely approximated by the frequency of the equivalent straight beam. Using the relation between the C-block and the straight beam and the definition of the C-block natural frequency (equation (19)), the first natural frequency of the C-block is

$$\omega_c = \frac{1{\cdot}758}{\pi n^2 R_n^2}\sqrt{\frac{D}{\rho}} = \frac{1{\cdot}758a}{\sqrt{3}\pi n^2 R_n^2}\sqrt{\frac{Y}{\rho_v}} \propto \left(\frac{a}{n^2 R_n^2}\right)\left(\sqrt{\frac{Y}{\rho_v}}\right), \tag{44}$$

where this expression has been simplified by assuming a cross-section of thickness $2a$. This equation demonstrates that increasing the stiffness, Y, or thickness, a, of the C-block, or decreasing its density, ρ_v, or radius, R_n, will increase the natural frequency. As expected, these conclusions match those from the investigation of the individual C-block, a more thorough discussion of which is contained in reference [24]. Unlike the individual C-blocks, the values of the natural frequencies also depend on the number of C-blocks in the series, n. Figure 4 shows that as the number of C-blocks is increased, the natural frequencies drop approximately proportional to n^2 for bending frequencies and proportional to n for extensional frequencies. The first natural frequency is primarily a bending frequency, and thus equation (44) shows the n^2 proportionality. As the number in series grows, and the equivalent straight bender approximation becomes more accurate, the n^2 and n proportionalities more accurately reflect the dependency of the dynamic model.

The comparison of experimental results from different actuators clearly shows the effect of the number in series on the natural frequencies. For example, Figure 15 shows the non-dimensional experimental frequency–amplitude response, λ_i, for three ceramic C-block actuators: an individual C-block [24], two in series, and four in series. The output deflection has been normalized to one at static displacements and the frequency has been non-dimensionalized using equation (19). Figure 15 shows that as the number in series

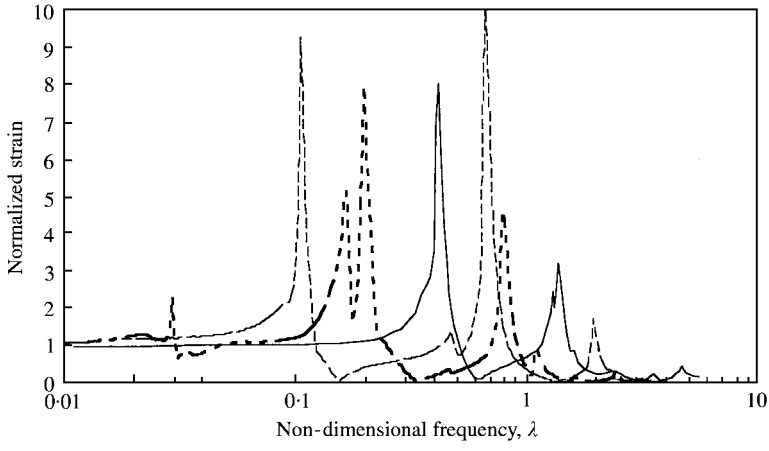

Figure 15. Comparison of C-block actuator dynamic frequency–amplitude response. The experimentally determined non-dimensional frequency–amplitude response of three C-block actuators (individual, two in series, and four in series) is shown. The original data are given in Figures 13 and 14 of this paper and in Figure 7 of reference [24]. The output strain is normalized with respect to the moment effectiveness: ——, individual C-block; – – – – – –, series of two C-blocks; - - - - -, series of four C-blocks.

increases, the natural frequency locations drop. For example, the first non-dimensional natural frequency, λ_1, of the individual C-block occurs at 0·426, while the first non-dimensional natural frequency of the series of two drops to 0·1269, and the first non-dimensional natural frequency of the series of four is the small peak at only 0·0298. Thus, larger arrays of C-blocks have correspondingly lower natural frequencies.

4.2. AMPLITUDE

In addition to the frequency, the amplitude of the C-block deflection (equation (36)) is dependent on the group of terms multiplying the frequency–amplitude model, and on the orthogonality constants contained within the square root. The multiplicative group of terms is

$$w_n \propto \frac{M^P R_n^2}{D} = \frac{d_{31} E_3 R_n^2}{2a} \propto \left(\frac{R_n^2}{a}\right)(d_{31}\, E_3), \tag{45}$$

where this expression has been simplified by assuming a cross-section of thickness $2a$. This collection of terms scales the output amplitude at all frequencies. This equation, and an examination of the experimental results, demonstrates that increasing the electric field, E_3, the piezoelectric constant, d_{31}, or the radius, R_n, or decreasing the thickness, a, of the C-block increases the output deflection. In addition to the parameters shown in equation (45), the deflection is dependent on the orthogonality constants. As shown in Figures 5 and 6, these constants tend to scale linearly with n. Thus, in general, the displacement of the C-block tip increases linearly with the number in series.

However, experimental results show that, in particular circumstances, the dependency of the deflection on n is more complex. For example, it is particularly interesting to compare the frequency–amplitude plots seen in Figure 15 from different actuators to demonstrate the effect of these constants. In the experimental results, the normalized displacement output at the first peak decreases as the number of C-blocks in series increases. With four in

series, the amplitude of the first peak is already relatively small, as seen in Figure 12. This is particularly interesting because, even with a small damping ratio, the strain amplitude around the first natural frequency is smoothed out, dropping only slightly below the static displacement amplitude. The small amount of damping effectively eliminates the dip to zero strain amplitude exhibited by the individual C-block. The explanation for this behavior is that, as the number of C-blocks in series grows, the first natural frequency becomes primarily a transverse mode, where the longitudinal orthogonality constant decreases and the transverse orthogonality constant increases. Thus, for the longitudinal mode measured, the amplitude peak at the first natural frequency is smaller than the second peak. This is significant because it shows that, as the C-block arrays get longer, the importance of the first natural frequency in longitudinal motion decreases. This means that, for long C-blocks, the actuator could be used for applications having a frequency range beyond the lower natural frequencies of the C-block without producing wide-amplitude deviations across the frequency spectrum.

5. CONCLUSION

This paper presented the investigation of the dynamic behavior of a generic C-block array architecture. A Hamiltonian energy method was utilized to derive an analytical frequency amplitude model for a generic C-block actuator. The transfer matrix method was used to reduce the model of a generic C-block actuator to a 6×6 matrix equation with two vector boundary conditions. Even though the derivation was complex, the final model is simple to use and depends only on parameters that can be measured or determined from the graphs in Figures 4–6. Through experimental validation with four distinctly different prototypes, this model was found to predict the first natural frequency to within an average of 2·93% and the amplitudes to within 3·19% for the ceramic prototypes and 8·42% for the polymeric prototypes.

From the model, it can be observed that as the number of C-blocks in series increases, the actuator reproduces both bending beam behavior and extensional rod behavior of an equivalent straight bender. A dynamically equivalent straight bender model was derived that predicts the natural frequency of the fourth mode to within 5% and the second mode to within 1% for more than 10 C-blocks in series. However, if the C-blocks are below 10 in series then the transfer matrix method should be employed.

From the parameter analysis based upon the models and experiments, it was determined that the natural frequencies of a C- block array can be increased by increasing C-block stiffness (square root effect), increasing thickness (linear effect), decreasing the radius (quadratic effect), decreasing the mass (square root effect), and decreasing the number in series (quadratic effect).

The amplitude can be increased by increasing the C-block radius (quadratic effect), increasing the number in series (linear effect), and decreasing the thickness (linear effect).

To simultaneously maximize both the bandwidth and amplitude, the engineer should strive to maximize the strain and Young's modulus and minimize the density. The number in series should also be minimized, although the importance of lower frequencies decreases as the number in series increases. This indicates that it may be possible to use any number of C-blocks in series for practical applications.

Thus, with the simple analytical models derived in this paper along with the insight gained from the straight bender and parameter analysis, it is possible to design and predict

the dynamic performance of a generic C-block actuator for a given application which requires a midrange piezoelectric actuator.

REFERENCES

1. B. Culshaw 1996 *Smart Structures and Materials*. Norwood, MA: Artech House.
2. D. Damjanovic and R. E. Newnham 1992 *Journal of Intelligent Material Systems and Structures* **3**, 190–208. Electrostrictive and piezoelectric materials for actuator applications.
3. R. Bamford, C. P. Kuo, R. Glaser and B. K. Wada 1995 in *AIAA/ASME/ASCE/AHS/ASC Structures, Structural Dynamics, and Materials Conference—Collection of Technical Papers*. New York: AIAA, 3278–3284. Long stroke percision PZT actuator.
4. D. K. Samak and I. Chopra 1996 *Smart Materials and Structures* **5**, 58–57. Design of high force, high displacement actuators for helicopter rotors.
5. K. Onitsuka, A. Dogan, J. F. Tressler, Q. XU, S. Yoshikawa and R. E. Newnham 1995 *Journal of Intelligent Material Systems and Structures* **6**, 447–455. Metal–ceramic composite transducer, the 'Moonie'.
6. E. F. Prechtl and S. R. Hall 1997 in *Smart Materials and Structures* 1997: *Smart Structures and Integrated Systems*. Bellingham, WA: SPIE, 158–182. Design of a high efficiency discrete servoflap actuator for helicopter rotor control.
7. J. Zhu, D. Wang, C.-J. Kirn and G. P. Carman 1996 in *Proceedings of the American Society of Mechanical Engineers Aerospace Division*, New York: ASME, 649–654. Development of a mesoscale actuation device.
8. T. Pandell and E. Garcia 1996 in *Proceedings of the American Society of Mechanical Engineers Aerospace Division*. New York: ASME, 627–648. Design of a piezoelectric caterpillar motor.
9. G. H. Haertling 1994 *American Ceramic Society Bulletin* **73**, 93–96. Ultra-high-displacement actuator.
10. S. R. Hall and E. F. Prechtl 1996 *Smart Materials and Structures* **5**, 26–34. Development of a piezoelectric servoflap for helicopter rotor control.
11. Face International 1996 *Thunder Sensors and Actuators* [brochure]. Available from Face International, 427 W. 35th St. Norfolk, VA 23508.
12. A. J. Moskalik and D. Brei 1997 *Journal of Intelligent Material Systems and Structures*, **8**, 571–587. Quasi-static behavior of individual C-block piezoelectric actuators.
13. J. S. N. Paine and Z. Chaudhry 1996 in *Proceedings of the American Society of Mechanical Engineers Aerospace Division*. New York: ASME, 511–516. The impact of amplification on efficiency and energy density of induced strain actuators.
14. A. J. Moskalik and D. Brei 1999 *Smart Materials and Structures* **8**, 531–543. Force–deflection behavior of piezoelectric C-block actuator arrays.
15. V. D. Kugel, S. Chandran and L. E. Cross 1997 in *Smart Structures and Materials* 1997: *Smart Materials Technologies*. Bellingham, WA: SPIE, 70–80. Comparative analysis of piezoelectric bending-mode actuators.
16. J. Kudva, P. Jardine, C. Martin and K. Appa 1996 in *Smart Structures and Materials* 1996: *Industrial and Commercial Applications of Smart Structures Technologies*. Bellingham, WA: SPIE, 10–16. Overview of the ARPA/WL 'Smart structures and materials development—smart wing' contract.
17. G. Washington 1996 *Smart Materials and Structures* **5**, 801–805. Smart aperture antennas.
18. A. Fukama, M. Yano, H. Tokuda, M. Ohki and R. Kizu 1994 *International Journal of Vehicle Design* **15**, 348–357. Development of piezo-electric actuators and sensors for electronically controlled suspension.
19. S. R. Thirupathi and N. G. Naganathan 1992 in *Robotics, Spatial Mechanisms, and Mechanical Systems*. New York: ASME, 233–241. Use of piezoceramic actuation for automotive active suspension mechanisms: a feasibility study.
20. H. Sumali and H. Cudney 1994 in *Proceedings of the 35th SDM Conference*. New York: AIAA, 1233–1241. An active engine mount with a piezoelectric stacked actuator.
21. D. K. Samak and I. Chopra 1993 in *Smart Structures and Materials* 1996: *Smart Structures and Intelligent Systems*. Bellingham, WA: SPIE, 225–237. A feasibility study to build a smart rotor: trailing edge flap actuation.
22. D. R. Martinez, T. D. Hinnerichs and J. M. Redmond 1996 *Journal of Intelligent Material Systems and Structures* **7**, 182–191. Vibration control for precision manufacturing using piezoelectric actuators.

23. J. ROJAS, C. LIANG and Z. J. GENG 1996 in *Smart Materials and Structures* 1996: *Industrial and Commercial Applications of Smart Structures Technologies*. Belligham, WA: SPIE, 373–384. Experimental investigation of active machine tool vibration control.
24. A. J. MOSKALIK and D. BREI 1999 *Journal of Vibration and Acoustics* **121**, 221–230. Analytical dynamic performance modeling for individual C-block actuators.
25. L. MEIROVITCH 1967 *Analytical Methods in Vibration*. New York: Macmillan.
26. M. S. QATU 1993 *International Journal of Solids and Structures* **20**, 2743–2756. Theories and analyses of thin and moderately thick laminated composite curved beams.
27. P. H. LARSON and J. R. VINSON 1993 in *Adaptive Structures and Material Systems*. New York: ASME, 277–285. On the analysis of adaptive shell structures employing piezoelectric materials.
28. E. PESTEL and F. A. LECKIE 1963 *Matrix Methods in Elastomechanics*. New York: McGraw-Hill.
29. X. ZENG, L. D. MITCHELL and W. X. LI 1991 in *Modal Analysis, Modeling, Diagnostics, and Control—Analytical and Experimental*. New York ASME. Quantification of the eigenfrequency extraction advantages of the Riccati transfer matrix method over the standard transfer matrix method.